MNRAS **000**, 1–14 (2019) Preprint 27 December 2019 Compiled using MNRAS LaTeX style file v3.0

Evolving pulsation of the slowly rotating magnetic β Cep star ξ^1 CMa

G.A. Wade*[1], A. Pigulski[2], S. Begy[1], M. Shultz[3], G. Handler[4], J. Sikora[5], H. Neilson[6], H. Cugier[2], C. Erba[3], A.F.J. Moffat[7], B. Pablo[8], A. Popowicz[9], W. Weiss[10], K. Zwintz[11]

[1] *Dept. of Physics & Space Science, Royal Military College of Canada, PO Box 17000 Station Forces, Kingston, ON, Canada K7K 0C6*
[2] *Instytut Astronomiczny, Uniwersytet Wrocławski, Kopernika 11, 51-622 Wrocław, Poland*
[3] *Dept. of Physics and Astronomy, University of Delaware, 217 Sharp Lab, Newark, DE 19716, USA*
[4] *Nicolaus Copernicus Astronomical Center, Bartycka 18, 00–716 Warszawa, Poland*
[5] *Dept. of Physics, Engineering Physics and Astronomy, Queen's University, 99 University Avenue, Kingston, ON K7L 3N6, Canada*
[6] *Dept. of Astronomy & Astrophysics, University of Toronto, 50 St. George Street, Toronto, ON M5S 3H4, Canada*
[7] *Dépt. de physique and Centre de Recherche en Astrophysique du Québec (CRAQ), Université de Montréal, C.P. 6128, Succ. Centre-Ville, Montréal, QC H3C 3J7, Canada*
[8] *American Association of Variable Star Observers, 49 Bay State Road, Cambridge, MA 02138, USA*
[9] *Silesian University of Technology, Institute of Automatic Control, Akademicka 16, Gliwice, Poland*
[10] *Institut für Astrophysik, Universität Wien, Türkenschanzstrasse 17, A-1180 Wien, Austria*
[11] *Institut für Astro- und Teilchenphysik, Universität Innsbruck, Technikerstrasse 25/8, A-6020 Innsbruck, Austria*

Accepted . Received ; in original form

ABSTRACT

Recent BRITE-Constellation space photometry of the slowly rotating, magnetic β Cep pulsator ξ^1 CMa permits a new analysis of its pulsation properties. Analysis of the two-colour BRITE data reveals the well-known single pulsation period of 0.209 d, along with its first and second harmonics. A similar analysis of SMEI and TESS observations yields compatible results, with the higher precision TESS observations also revealing several low-amplitude modes with frequencies below 5 d^{-1}; some of these are likely g modes. The phase lag between photometric and radial velocity maxima - equal to 0.334 cycles - is significantly larger than the typical value of 1/4 observed in other large-amplitude β Cep stars. The phase lag, as well as the strong dependence of phase of maximum light on wavelength, can be reconciled with seismic models only if the dominant mode is the fundamental radial mode. We employ all published photometric and radial velocity measurements, spanning over a century, to evaluate the stability of the pulsation period. The $O-C$ diagram exhibits a clear parabolic shape consistent with a mean rate of period change $\dot{P} = 0.34 \pm 0.02$ s/cen. The residuals from the best-fit parabola exhibit scatter that is substantially larger than the uncertainties. In particular, dense sampling obtained during the past ~20 years suggests more complex and rapid period variations. Those data cannot be coherently phased with the mean rate of period change, and instead require $\dot{P} \sim 0.9$ s/cen. We examine the potential contributions of binarity, stellar evolution, and stellar rotation and magnetism to understand the apparent period evolution.

Key words: Stars: pulsation – Stars : rotation – Stars: massive – Instrumentation : spectropolarimetry – Stars: magnetic fields

1 INTRODUCTION

ξ^1 CMa (HR 2387 = HD 46328 = HIP 31125 = MCW 441 = ADS 5176A) is a bright ($V = 4.3$ mag), apparently single, B0.5 subgiant located near the middle of its main sequence evolution (e.g. Niemczura & Daszyńska-Daszkiewicz 2005; Shultz et al. 2017). It has long been known to exhibit large-amplitude β Cep radial pulsations with a period of roughly $P = 0.20958$ d (4.77 d^{-1}; e.g. McNamara 1953; Williams 1954; Heynderickx 1992; Saesen et al. 2006).

---

* E-mail: wade-g@rmc.ca

Hubrig et al. (2009) reported the star to be magnetic. Shultz et al. (2017) performed a detailed determination of the star's physical parameters, finding $T_{\text{eff}} = 27{\pm}1$ kK, $\log g = 3.78 \pm 0.07$, and an age of 11.1 ± 0.7 Myr. At an inferred mass of 14.2 ± 0.4 $\mathrm{M}_{\odot}$, this implies that ξ^1 CMa has completed three-quarters of its main sequence evolution.

Analysis of high resolution spectropolarimetry obtained between 2000 – 2017 led Shultz et al. (2017) to conclude that the star's rotation period is remarkably long, over 30 years. In particular, Shultz et al. (2017) (see as well Shultz et al. 2018) demonstrated that previous claims of much shorter rotation periods were unable to explain the magnetic observations. Shultz et al. (2018) discovered the presence of unexpected crossover signatures in Stokes V profiles of ξ^1 CMa obtained near the phase of null longitudinal field. They demonstrated that the combination of radial pulsation and departures from a dipole magnetic field geometry could explain the presence of this novel and unexpected "radial crossover" effect.

Shultz et al. (2017) also examined the behaviour of the radial-velocity (RV) pulsations of the star over a span of 17 yr. They demonstrated that a constant pulsation period was unable to phase those data coherently, and consequently inferred that the period was increasing at a rate of 0.96 s/cen. This result is qualitatively consistent with earlier reports of period instability of ξ^1 CMa. Jerzykiewicz (1999), in his summary of period evolution of β Cep stars, cites a rate of period change of 0.37 ± 0.05 s/cen reported by Pigulski (1992a). Neilson & Ignace (2015) used those results to test the influence of rotation and convective core overshoot on models of massive star evolution, finding that the measured rate of period change of ξ^1 CMa was in good agreement with that predicted by models under the constraints applied by the physical parameters of Shultz (2016); Shultz et al. (2017).

Real or apparent pulsation period evolution can be the consequence of a number of phenomena, including binarity and stellar evolution. For example, Odell (1984, 2012) reported that the β Cep star BW Vul exhibits complex period variability that Odell (2012) concluded is best understood as a piecewise linear ephemeris, corresponding to a constant period interrupted every few decades by an abrupt period change. A number of studies have considered the role of stellar evolution and binarity in understanding pulsation period changes (Neilson et al. 2016). Eddington (1919) conducted the first test by considering the rate of period change for the prototype Cepheid, δ Cephei, and showed that the rate of period change was inconsistent with energy generation from gravitational contraction. More recently, numerous works have used period change measurements to test evolution of Cepheids such as Polaris, δ Cep, and l Car (Neilson et al. 2012, 2016; Neilson 2014; Fadeyev 2015; Anderson 2018). Anderson et al. (2015) considered the period change of δ Cep as potential evidence for an undetected close companion. Period change due to evolutionary effects has not been examined in detail for RR Lyrae stars; however Koopmann et al. (1994) and Kunder et al. (2011) made predictions of period change from stellar evolution models and found some consistency with observations. This has been confirmed by Le Borgne et al. (2007) and Percy & Tan (2013). The light-time effect due to binary companions appears to be one of the origins of apparent period changes for the β Cephei stars (Pigulski & Boratyn 1992; Pigulski 1992b, 1993).

In this paper we revisit (a) the pulsation frequency spectrum and (b) the evolution of the fundamental pulsation period of ξ^1 CMa. We report new two-colour BRITE photometry of the star which we analyse in tandem with SMEI photometry to search for evidence of additional pulsation frequencies. We then revisit the period evolution reported by Jerzykiewicz (1999) and Shultz et al. (2017) using all published photometric and radial velocity (RV) measurements of ξ^1 CMa, spanning over 100 years.

2 SPACE PHOTOMETRIC OBSERVATIONS

2.1 BRITE-Constellation photometry

ξ^1 CMa was observed by BRITE-Constellation (Weiss et al. 2014; Pablo et al. 2016) during its run in the Canis Major/Puppis I field between October 26, 2015, and April 18, 2016. The observations were taken by three BRITE satellites, red-filter BRITE-Heweliusz (BHr) and BRITE-Toronto (BTr), and blue-filter BRITE-Lem (BLb), in 'chopping mode' (Pablo et al. 2016). A short summary of the characteristics of the BRITE data is given in Table 2. The photometry was obtained by means of the photometric pipeline described by Popowicz et al. (2017) and then corrected for instrumental effects according to the procedure described by Pigulski (2018). The complete reduced BRITE dataset spans 173.5 days and consists of 152 112 photometric measurements.

2.2 SMEI photometry

The Solar Mass Ejection Imager (SMEI) experiment (Eyles et al. 2003; Jackson et al. 2004) was placed on-board of the Coriolis spacecraft and was aimed at measuring sunlight scattered by free electrons of the solar wind. We used photometry of ξ^1 CMa obtained between 2003 and 2010 and available through the University of California San Diego (UCSD) web page[1]. The SMEI time series are affected by long-term calibration effects, especially a repeatable variability with a period of one year. The raw SMEI UCSD photometry of ξ^1 CMa were corrected for the one-year variability by subtracting an interpolated mean light curve, which was obtained by folding the raw data with the period of one year, calculating median values in 200 intervals in phase, and then interpolating between them. In addition, the worst parts of the light curve and outliers were removed. The data points were also assigned individual uncertainties calculated using the scatter of the neighbouring data. Then, a model consisting of the dominant pulsation frequency (4.77 d^{-1}) and its detectable harmonics was fitted to the data. Finally, the low-frequency instrumental variability was filtered out by subtracting a trend using residuals from the fit. The last two steps were iterated several times. The SMEI dataset that we analysed spans 2885 days and consists of 25 581 photometric measurements.

---

[1] http://smei.ucsd.edu/new_smei/index.html

Table 1. New (2018-2019) radial velocity measurements of ξ^1CMa. These data are described in Sect. 3.

HJD-2458000	RV (km s^{-1})	HJD-2458000	RV (km s^{-1})	HJD-2458000	RV (km s^{-1})
148.75321	11.8 ± 0.7	557.77240	39.9 ± 1.3	559.79702	14.5 ± 0.6
148.75429	11.6 ± 0.7	557.77349	40.1 ± 1.3	559.81117	20.4 ± 0.8
148.75537	10.0 ± 0.7	557.77459	40.0 ± 1.3	559.81230	20.9 ± 0.8
148.75645	10.2 ± 0.7	557.77569	40.0 ± 1.3	559.81342	21.5 ± 0.8
148.97144	9.5 ± 0.7	557.83743	16.4 ± 0.7	559.81455	21.9 ± 0.8
148.97252	9.3 ± 0.7	557.83856	15.9 ± 0.7	559.82356	26.1 ± 0.9
148.97360	9.8 ± 0.7	557.83969	15.4 ± 0.7	559.82467	26.6 ± 0.9
148.97468	10.0 ± 0.7	557.84081	15.0 ± 0.7	559.82577	27.1 ± 0.9
150.79889	33.0 ± 0.9	557.84309	14.0 ± 0.6	559.82688	27.7 ± 0.9
150.79997	32.3 ± 0.9	557.84419	13.5 ± 0.6	560.71247	40.0 ± 1.3
150.80105	32.3 ± 0.9	557.84529	13.1 ± 0.6	560.71357	40.5 ± 1.3
150.80213	31.7 ± 0.9	557.84639	12.6 ± 0.6	560.71467	39.7 ± 1.3
153.85512	19.0 ± 0.8	557.84869	11.8 ± 0.6	560.71577	39.6 ± 1.3
153.85620	18.9 ± 0.8	557.84984	11.5 ± 0.6	560.71862	39.1 ± 1.3
153.85728	19.2 ± 0.8	557.85100	11.1 ± 0.6	560.71973	38.9 ± 1.3
153.85835	20.0 ± 0.8	557.85214	11.4 ± 0.6	560.72083	39.0 ± 1.2
154.70789	25.1 ± 0.9	559.76216	7.2 ± 0.5	560.72193	38.7 ± 1.3
154.70898	25.4 ± 0.9	559.76327	7.3 ± 0.5	560.72359	37.9 ± 1.2
154.71008	26.1 ± 0.8	559.76438	7.3 ± 0.5	560.72470	37.5 ± 1.2
154.71119	26.4 ± 0.8	559.76548	7.3 ± 0.5	560.72580	37.2 ± 1.2
154.91334	23.4 ± 0.8	559.76721	7.5 ± 0.5	560.72690	36.8 ± 1.2
154.91444	23.6 ± 0.8	559.76837	7.6 ± 0.5	560.76130	21.8 ± 0.8
154.91554	24.2 ± 0.8	559.76953	7.6 ± 0.5	560.76242	20.8 ± 0.8
154.91664	24.7 ± 0.8	559.77068	7.9 ± 0.5	560.76352	20.3 ± 0.8
156.76397	9.5 ± 0.6	559.77267	8.1 ± 0.5	560.76463	19.8 ± 0.8
156.76505	9.5 ± 0.6	559.78286	10.0 ± 0.6	563.74274	6.3 ± 0.5
156.76613	10.2 ± 0.7	559.78396	10.3 ± 0.6	563.74385	6.2 ± 0.5
156.76721	12.1 ± 0.7	559.78506	10.5 ± 0.6	563.74496	7.2 ± 0.5
156.91427	16.5 ± 0.8	559.78616	10.9 ± 0.6	563.74607	7.3 ± 0.5
156.91535	16.1 ± 0.8	559.78814	11.5 ± 0.6	564.84618	22.6 ± 0.8
156.91643	15.6 ± 0.8	559.78928	11.9 ± 0.6	564.84728	23.2 ± 0.8
156.91751	15.1 ± 0.7	559.79043	12.2 ± 0.6	564.84839	23.7 ± 0.9
557.76676	39.5 ± 1.2	559.79158	12.7 ± 0.6	564.84949	24.2 ± 0.9
557.76787	39.7 ± 1.2	559.79356	13.3 ± 0.6	564.85109	24.8 ± 0.9
557.76897	39.8 ± 1.3	559.79471	13.7 ± 0.6	564.85220	25.4 ± 0.9
557.77007	39.9 ± 1.3	559.79586	14.1 ± 0.6	564.85331	26.0 ± 0.9
				564.85443	26.5 ± 0.9

Table 2. Space photometry of ξ^1 CMa. RSD and DT stand for residual standard deviation and detection threshold defined as signal-to-noise (S/N) equal to 4 in the frequency spectrum.

Satellite ID	Time span [d]	$N_{\rm obs}$	RSD [mmag]	DT [mmag]
BLb	96.7	31 255	19.2	0.93
BTr	156.5	64 883	5.4	0.18
BHr	166.9	55 974	14.4	0.53
BTr + BHr	173.5	120 857	10.6	0.17
SMEI	2884.7	25 581	10.6	0.32
TESS	21.8	14 814	0.2	0.03

2.3 TESS photometry

The primary goal of the NASA's TESS mission (Ricker et al. 2014, 2015) is the detection of planets by means of the transit method. TESS observations cover almost the entire sky, excluding only the regions with low Galactic latitudes ($|b| < 6°$). Observations are carried out with a 30-min cadence, but selected stars, including ξ^1 CMa, are observed with a shorter, 2-min cadence. The star was observed with TESS camera #2 in Sector 6. The observations spanned 21.8 d between December 11, 2018, and January 7, 2019, and consisted of 15 678 data points. In the subsequent analysis (Sect. 2.4) we used SAP fluxes and removed all data points with quality flag different from 0.

2.4 Frequency analysis

Fourier analysis with prewhitening was performed on the BRITE photometry using the Period04 package (Lenz & Breger 2005). We combined the BTr and BHr data and analyzed them as a single dataset. One significant frequency was detected at 4.771491(7) d^{-1} (amplitude of 14.8 mmag, corresponding to a period of 0.2095781(3) d), along with its first two harmonics (with amplitudes of 2.0 and 0.6 mmag, respectively). The original and prewhitened (up to the second harmonic) Fourier amplitude spectra of the red BRITE data are illustrated in Fig. 1. As is evident in Fig. 1, the BRITE data reveal no evidence for new independent pulsation frequencies with amplitudes larger than about 0.17 mmag. Analysis of the blue BRITE data yields compatible results, but with higher uncertainties and upper limits (0.93 mmag).

A similar analysis was performed on the SMEI data (Fig. 1). The fundamental pulsation frequency 4.771517(2) d^{-1} (amplitude of 11.7 mmag, corresponding to a period of 0.2095770(1) d) was clearly detected. No significant non-instrumental signal was detected after prewhitening with the fundamental frequency and its first two harmonics (amplitudes of 1.5 mmag and 0.9 mmag, respectively). However, the fundamental pulsation frequency determined using the SMEI data is somewhat higher than that derived using the BRITE data. This difference is consistent with the reported evolution of the pulsation period of ξ^1 CMa, and will be discussed further below. The detection threshold of the SMEI data, taking into account uncertainties associated with the removal of long-term trends, is about 0.3 mmag.

Finally, we analyzed TESS photometry of ξ^1 CMa. With the exceptionally low detection threshold of about 0.03 mmag (Table 2) we were able to detect not only the dominant frequency (at 4.771483(6) d^{-1}, with an amplitude of 12.8 mmag), but also its four lowest harmonics. In addition (Fig. 2), the frequency spectrum shows extra power below ~5 d^{-1}. Several significant peaks with amplitudes below 0.12 mmag can be identified. They may correspond to both p and/or g modes. The detailed analysis and possible seismic modeling with the use of these frequencies is, however, beyond the scope of this paper.

3 SPECTROPOLARIMETRIC OBSERVATIONS AND RADIAL VELOCITIES

In addition to the ESPaDOnS RVs published by Shultz et al. (2017), we have included new RV measurements obtained from follow-up ESPaDOnS observations in 2018 and 2019[2]. Eight spectropolarimetric sequences were obtained in 2018; the magnetic analysis of these data were described by Shultz et al. (2018). A further 19 sequences were obtained in 2019; the magnetic analysis will be presented by Erba et al. (in prep.).

ESPaDOnS is an echelle spectropolarimeter with a high resolving power ($\lambda/\Delta\lambda \sim 65,000$), with a wavelength range of about 370 nm to 1000 nm, mounted at the Cassegrain focus of the 3.6 m Canada-France-Hawaii Telescope (CFHT). The instrument properties and data reduction were described in detail by Wade et al. (2016). Each spectropolarimetric sequence consists of 4 differently spectra. The 2019 observations are essentially identical to the 2018 observations described by Shultz et al. (2018), with a mean peak signal-to-noise (S/N) per spectral pixel of about 400 in the individual intensity spectra. In the case of ξ^1 CMa the exposure time per individual spectrum (72 s) is a much lower fraction of the pulsation period than the combined 8 minute exposure-plus-readout time of a full sequence (0.004% vs. 0.027%), therefore individual spectra were used for RV measurements, thus yielding 32 measurements in 2018 and 76 measurements in 2019. RVs were measured from the weighted means of the centres-of-gravity across multiple unblended spectral lines, using the same method and line list described by Shultz et al. (2017).

4 EVOLUTION OF THE PULSATION PERIOD FROM 1906-2017

To investigate the behaviour of the pulsation period of ξ^1 CMa we have constructed an O – C diagram using all available spectroscopic and photometric observations. Since both light and radial velocity can be described by a single periodicity, the times of maximum light (and radial velocity) were derived by fitting a function of the form

$$\sum_{m=1}^{N} A_m \sin(2\pi m f t + \phi_m), \tag{1}$$

to the light or radial velocity time-series. In this equation, f stands for the pulsation frequency, t is the time elapsed from the initial epoch, while A_m and ϕ_m are respectively semi-amplitudes and phases of the consecutive harmonic terms. Depending on the data, the fitted model included all detectable harmonics, up to $N = 5$. The harmonics account for deviations from the sinusoidal shape of the light or radial velocity curve. The times of maximum summarized in Tables 3 and 4 correspond to the maximum of the fit given by Eq. (1), that is, including all detectable harmonics. In our analysis, all dates are given as HJD at the mid-time of exposures.

4.1 Radial velocity data

The radial velocity data consist of a rich, high-quality data set of spectroscopic measurements obtained in the years 2000 – 2019 and five archival data sets, which extend the study of period changes to over a century. The 2000 – 2016 spectroscopy was used by Shultz et al. (2017) and Begy et al. (2018) to conclude that the pulsation period of ξ^1 CMa changes with the constant rate of +0.9 ± 0.1 s/cen. The archival data include radial velocities published by Frost et al. (1926) (these are the corrected discovery data of Frost (1907) plus one additional spectrum), Henroteau (1921), Campbell & Moore (1928), and McNamara (1955, 1956). All data are available and were used to derive the times of maximum presented in Table 3. Heliocentric corrections were applied to all data for which the reported time was given in Julian Days. The 2000 – 2016 spectroscopy was split into 11 subsets, usually corresponding to a single observing season. In case the number of observations was small, data from adjacent seasons were combined.

4.2 Photometric data

The archival photometry of ξ^1 CMa includes ground-based observations of Williams (1954), van Hoof (1962), Watson (1971), Shobbrook (1973), and Heynderickx (1992). In addition, we used Strömgren uy photometry obtained at Fairborn Observatory in 2018 by one of us (G.H.). Surprisingly, the star was frequently observed from space. The data sets we

---

[2] Program codes and 18AC19 and 19AC20.

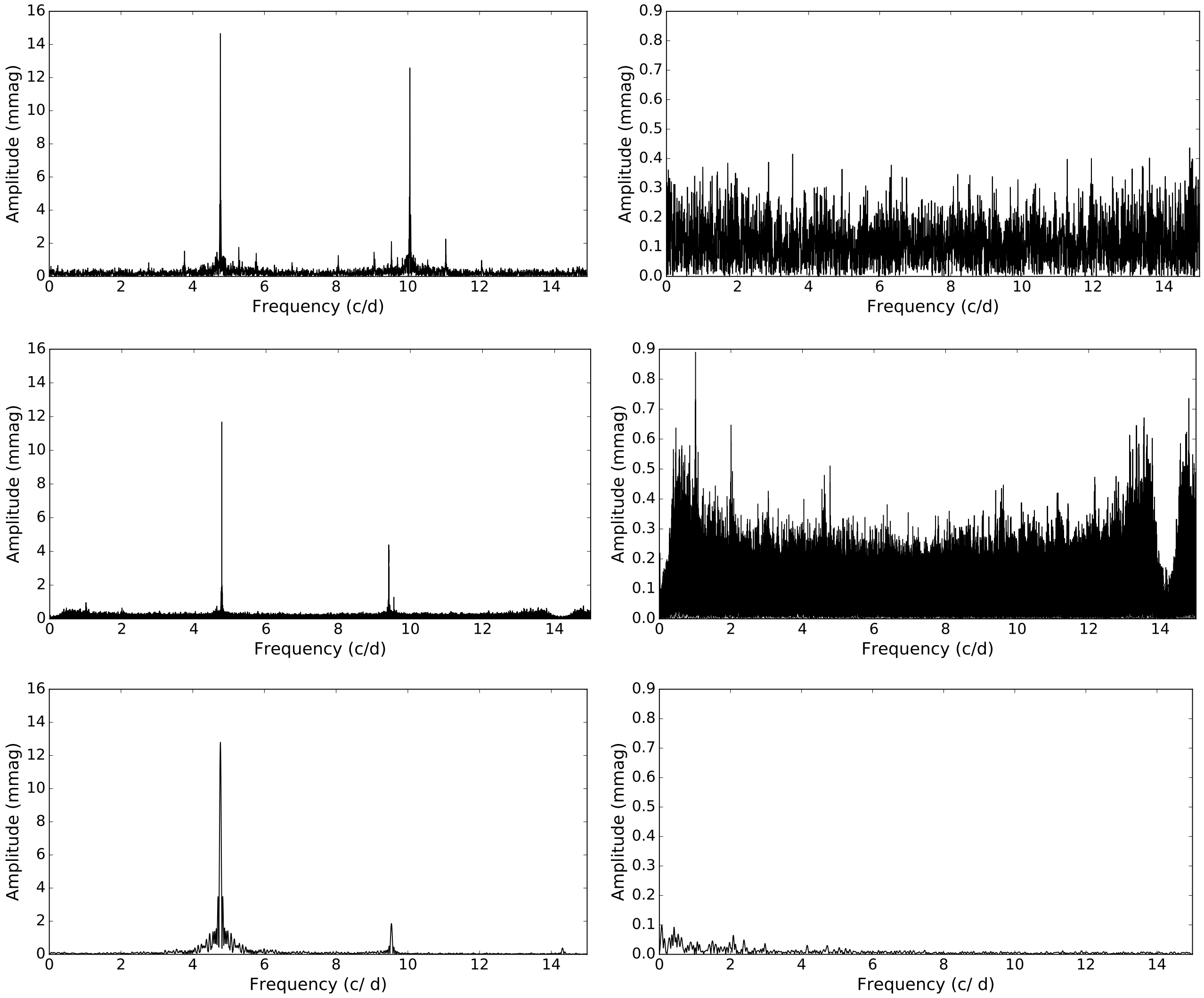

Figure 1. Fourier amplitude spectra of BTr+BHr data (upper frames) and SMEI data (lower frames) in mmag. *Upper left:* BTr+BHr data. *Upper right:* Spectrum of residuals following prewhitening with the fundamental frequency of 4.771491 d^{-1} and the first two harmonics. *Middle left:* Orbit-averaged SMEI data. *Middle right:* Spectrum of residuals following prewhitening with the fundamental frequency of 4.771517 d^{-1} and its first two harmonics. *Bottom left:* TESS data. *Lower right:* Spectrum of residuals following prewhitening with the fundamental frequency of 4.771483(6) d^{-1} and its first four harmonics. In the BRITE and SMEI residuals, the peaks at 1 and 2 d^{-1} are instrumental, as are peaks between 3 and 5 d^{-1}.

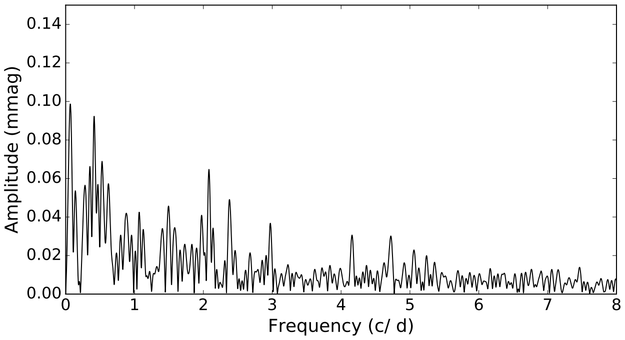

Figure 2. Fourier amplitude spectra of TESS sector 6 photometry showing weak peaks at low frequencies.

used include ultraviolet (UV) photometry from the TD-1A (Beeckmans & Burger 1977; Burger et al. 1980) and ANS (Lesh & Wesselius 1979) satellites and the optical-domain data from Hipparcos, BRITE (Sect. 2.1), SMEI (Sect. 2.2), and TESS (Sect. 2.3).

4.2.1 *Effective wavelengths*

In the presence of phase lags between the times of maximum in different photometric bands (Sect. 4.2.2), it became necessary to derive effective wavelengths for the passbands used in the observations of ξ^1 CMa. They were defined with the

Table 3. Times of maximum radial velocity for ξ^1 CMa. Columns give HJD of maximum RV, the number of cycles before/since the reference ephemeris, the inferred O-C, the source of the data, the number of observations, and any notes or comments.

$T_{\rm max}-$ HJD 2 400 000	E	(O−C) [d]	Source of data	$N_{\rm obs}$	Notes, comments
17221.336(10)	−114874	+0.06029	Frost et al. (1926)	5	1905 – 1906
19523.709(10)	−103888	+0.03734	Campbell & Moore (1928)	5	1909 – 1913
22697.054(10)	−88746	−0.01448	Henroteau (1921)	7	best of 1921 only
34439.0916(11)	−32718	−0.06859	McNamara (1955)	45	1952 – 1953
34816.1163(22)	−30919	−0.07022	McNamara (1956)	18	1954
51624.74742(39)	49284	−0.02292	Shultz et al. (2017)	51	Feb/Apr 2000
51888.60434(22)	50543	−0.02156	Shultz et al. (2017)	52	Dec 2000
51949.17159(23)	50832	−0.02163	Shultz et al. (2017)	51	Feb 2001
52233.98574(24)	52191	−0.02058	Shultz et al. (2017)	58	Nov 2001
52580.41476(73)	53844	−0.01986	Shultz et al. (2017)	10	Oct/Nov 2002
52989.29838(24)	55795	−0.01804	Shultz et al. (2017)	71	Dec 2003
53078.99670(25)	56223	−0.01804	Shultz et al. (2017)	60	Mar 2004
53278.30372(30)	57174	−0.01732	Shultz et al. (2017)	39	Sep/Oct 2004
55180.42624(24)	66250	−0.00204	Shultz et al. (2017)	79	Jan 2008 – Dec 2010
56308.58266(25)	71633	−0.00947	Shultz et al. (2017)	56	Feb 2012 – Jan 2014
57805.59816(24)	78776	+0.02717	Shultz et al. (2017)	85	Feb/Mar 2017
58560.28537(11)	82377	+0.03301	This paper	77	Mar 2019

following expression:

$$\lambda_{\rm eff} = \frac{\int_{\lambda_1}^{\lambda_2} \lambda S(\lambda) T_1(\lambda) T_2(\lambda) T_3(\lambda) d\lambda}{\int_{\lambda_1}^{\lambda_2} S(\lambda) T_1(\lambda) T_2(\lambda) T_3(\lambda) d\lambda}, \qquad (2)$$

where $S(\lambda)$ represents a model spectrum with $T_{\rm eff} = 27500$ K, $\log g = 3.75$ taken from the OSTAR2002 grid of models (Lanz & Hubeny 2003). The model parameters are close to the values derived for ξ^1 CMa by Shultz et al. (2017). The variables $T_1(\lambda)$, $T_2(\lambda)$, and $T_3(\lambda)$ (all included optionally) are filter transmission curves, detector sensitivity curves, and (for ground-based observations) the atmosphere transmission curves. Values of λ_1 and λ_2 were chosen to encompass the non-zero values of the sensitivity and transmission curves. Details concerning T_1, T_2, and T_3 are as follows:

- Shobbrook (1973): T_1 was Johnson V (the author used Corning 3384 filter which defines V band and an EMI 8094S photomultiplier with a S-11 photocathode, similar to that used in a 1P21 photmultiplier, which defines V), that is, a combination of filter transmission and detector sensitivity, taken from ADPS[3] (Moro & Munari 2000). For T_2 we took the extinction curve (twice as large as in La Silla; see Geneva photometry below). The same combination of T_1 and T_2 was adopted for the data published by Williams (1954) and van Hoof (1962).
- Watson (1971): T_1 was Newell v band transmission taken from ADPS, T_2 was the same as for Shobbrook (1973).
- TD-1A: T_1: Passband centres and effective widths were taken from the HEASARC web page[4]; shapes were approximated by an $\exp(-(\Delta\lambda/\sigma)^4)$ function. T_2, corresponding mainly to the detector response, was estimated for each TD-1A passband from fig. 8 of Boksenberg et al. (1973).
- ANS: T_1: Instrument response was taken from van Duinen et al. (1975).
- Geneva: Filter transmission curves T_1 were taken from ADPS; T_2 was S-11 photocatode QE curve[5]. As T_3, the La Silla extinction coefficient dependence was taken[6].
- Hipparcos: T_1: The passband as defined by Bessell (2000) was used.
- SMEI: For T_1 we adopted the typical E2V Technologies standard front-illuminated CCD sensitivity curve[7] because it seems to be similar to the description of the E2V CCD05-30-231A chip, given by Eyles et al. (2003).
- BRITE: T_1: The BRITE filter transmission curves from Weiss et al. (2014). T_2: Kodak KAI-11002 sensitivity curve from the product sheet[8].
- Fairborn Observatory ground-based observations in Strömgren u and y filters. For T_1 the transmissions curves for Strömgren u and y filters from ADPS were taken. For T_2 and T_3 the QE curve from Strassmeier et al. (1997) for the Thorn-EMI 9124QB photomultiplier and the La Silla extinction were used, respectively.
- TESS: The TESS curve, including both the sensitivity of the detector (Ricker et al. 2015) and the filter transmission curve, has been taken from the NASA's High Energy Astrophysics Science Archive Research Center web page[9].

The calculated effective wavelengths are given in Table 4.

---

[3] http://ulisse.pd.astro.it/Astro/ADPS/

[4] https://heasarc.gsfc.nasa.gov/W3Browse/all/td1.html

[5] http://www.r-type.org/pdfs/9531.pdf

[6] https://www.eso.org/sci/observing/tools/Extinction.html

[7] https://www.e2v.com/content/uploads/2017/08/ccdtn101.pdf

[8] http://www.onsemi.com/pub/Collateral/KAI-11002-D.PDF

[9] https://heasarc.gsfc.nasa.gov/docs/tess/data/tess-response-function-v1.0.csv

Table 4. Times of maximum light and related information for ξ^1 CMa. Columns give HJD of maximum light, correction to the HJD of maximum light in the visual domain (Eq. 3), the number of cycles before/since the reference ephemeris, the inferred O-C, the passband, the effective wavelength, the source of the data, the number of observations, and any notes or comments.

$T_{\rm max}^{\rm obs}-$ HJD 2 400 000	$C_{\rm Vis}$ [d]	E	(O−C) [d]	Passband(s)	$\lambda_{\rm eff}$ [nm]	Source of data	$N_{\rm obs}$	Notes, comments
34719.3697(38)	−0.0019	−31381	+0.0052	yellow	547	Williams (1954)	99	data read off the figures
37658.0342(15)	−0.0019	−17359	+0.0020	Y	547	van Hoof (1962)	unkn.	combined 13 $T_{\rm max}$
40562.9555(13)	−0.0013	−3498	−0.0021	Newell v	533	Watson (1971)	unkn.	from Shobbrook (1973)
41296.0514(6)	−0.0019	0	−0.0019	yellow	547	Shobbrook (1973)	562	original $T_{\rm max}$
41406.911(2)	—	529	−0.0058	155 – 275	214	Beeckmans & Burger (1977)	8	TD-1A
42867.8747(40)	—	7500	+0.0071	155, 180, 220	184	Lesh & Wesselius (1979)	25	ANS
42867.8727(40)	—	7500	+0.0051	250, 330	289	Lesh & Wesselius (1979)	25	ANS
47504.3265(10)	+0.0061	29623	+0.0262	Geneva U	348	Heynderickx (1992)	203	
47504.3292(11)	+0.0040	29623	+0.0268	Geneva B_1	401	Heynderickx (1992)	203	
47504.3300(10)	+0.0032	29623	+0.0268	Geneva B	419	Heynderickx (1992)	203	
47504.3305(12)	+0.0022	29623	+0.0263	Geneva B_2	446	Heynderickx (1992)	202	
47504.3342(17)	−0.0013	29623	+0.0265	Geneva V_1	534	Heynderickx (1992)	204	
47504.3326(19)	−0.0014	29623	+0.0248	Geneva V	535	Heynderickx (1992)	202	
47504.3359(18)	−0.0028	29623	+0.0267	Geneva G	570	Heynderickx (1992)	200	
48380.3596(13)	+0.0004	33803	+0.0280	$H_{\rm p}$	490	Hipparcos	216	
52992.3066(7)	−0.0046	55809	+0.0515	SMEI	615	SMEI (UCSD)	5116	SMEI data, part 1
53592.1155(6)	−0.0046	58671	+0.0553	SMEI	615	SMEI (UCSD)	5116	SMEI data, part 2
54123.6040(8)	−0.0046	61207	+0.0604	SMEI	615	SMEI (UCSD)	5116	SMEI data, part 3
54656.5586(7)	−0.0046	63750	+0.0645	SMEI	615	SMEI (UCSD)	5116	SMEI data, part 4
55252.1769(7)	−0.0046	66592	+0.0692	SMEI	615	SMEI (UCSD)	5117	SMEI data, part 5
57367.6476(3)	+0.0030	76686	+0.0924	BRITE blue	424	this paper	31255	BLb
57384.8364(11)	−0.0019	76768	+0.0911	Strömgren y	546	this paper	494	APT (Fairborn)
57385.0417(5)	+0.0060	76769	+0.0947	Strömgren u	345	this paper	501	APT (Fairborn)
57401.60040(10)	−0.00415	76848	+0.08683	BRITE red	604	this paper	120857	BHr + BTr
58479.250031(7)	—	81990	+0.103386	TESS	733	TESS	14812	Sector 6, camera #2

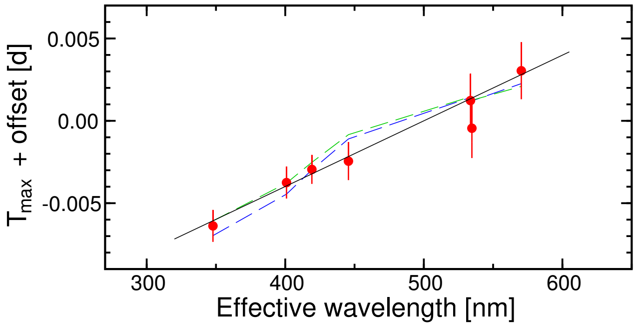

Figure 3. The times of maximum light derived from the Geneva photometry (Heynderickx 1992) in the visual domain (red points). The linear coefficient of the fitted line corresponds to $A_{\rm Vis}$ = $(+3.99 \pm 0.33) \times 10^{-5}$ d (nm)$^{-1}$. The dashed lines represent the theoretical dependences for the fundamental radial mode in two BG models with M = 14 $M_\odot$, $T_{\rm eff}$ = 27 kK, $\log g$ = 3.74, and ξ = 2 km s^{-1} (blue) and 10 km s^{-1} (green); see Sect. 4.4 for explanation.

4.2.2 Correction for the phase lag between photometric bands

The radial velocities of ξ^1 CMa were derived from the optical spectra and the analysis rarely included hydrogen lines. Therefore, systematic effects related to the velocity gradient in the atmosphere and non-adiabaticity, resulting in the phase lag between hydrogen and other lines, called van Hoof effect (van Hoof & Struve 1953; Mathias et al. 1991), is probably negligible in the case of ξ^1 CMa. On the other hand, the lack of phase lag cannot be assumed for photometric data, especially for a radially pulsating star with large amplitude like ξ^1 CMa. There are two multicolour data sets, which potentially enable to check if the phase lags are observed for ξ^1 CMa. The first one is the UV TD-1A photometry of ξ^1 CMa in four bands published by Burger et al. (1980), the other one is the seven-band Geneva photometry of Heynderickx (1992)[10]. In both data sets, the observations in all passbands are simultaneous. The effective wavelengths of these 11 passbands range between 151 and 570 nm. The Geneva photometry covers a wider wavelength range and is of better quality than the very scarce (8 data points only) TD-1A time-series. Due to the scarcity, the latter data set cannot be used to conclusively discuss the phase lags in the UV. The situation is much better for the Geneva data. The derived times of maximum light obtained from the Geneva data are plotted against the effective wavelengths of the passbands in Fig. 3. There is a clear dependence of the time of maximum light on $\lambda_{\rm eff}$ — the longer the wavelength, the later the time of maximum occurs. A least-squares fit gives the rate of the time of maximum lag $A_{\rm Vis} = (+3.99 \pm 0.33) \times 10^{-5}$ d (nm)$^{-1}$. The derived value of $A_{\rm Vis}$ translates into a difference in the time of maximum light equal to 0.0090 d = 13 min or 7 per cent of the pulsation period in the full range of the effective wavelengths covered by the Geneva filters (348 – 570 nm). Because simultaneous UV and visual data for ξ^1 CMa do

---

[10] Kindly provided by Gerald Handler.

not exist, the phase-lag corrections cannot be applied to the UV data. Consequently, we do not use the UV data in the fits shown in Fig. 4 (although they are shown for reference). Similarly, the phase lag is not extrapolated and the time of maximum not corrected for the TESS passband. The effect of phase (or times-of-maximum) lag has to be taken into account to properly use photometric data obtained in different passbands in the O − C diagram. These corrections to the times of maximum light in the visual domain, $C_{\rm Vis}[{\rm d}] = A_{\rm Vis}(500 - \lambda_{\rm eff})$, where $\lambda_{\rm eff}$ is in nm, were added to the observed times of maximum light, $T^{\rm obs}_{\rm max}$:

$$T^{\rm corr}_{\rm max} = T^{\rm obs}_{\rm max} + C_{\rm Vis} \qquad (3)$$

before the O − C values were calculated. Both $T^{\rm obs}_{\rm max}$ and $C_{\rm Vis}$ are reported in Table 4. The values of $T^{\rm corr}_{\rm max}$ were subsequently used to calculate the values of O − C according to the ephemeris, taken from Shobbrook (1973):

$$T_{\rm max} = {\rm HJD}2441296.0514 + 0.2095755 \times E, \qquad (4)$$

where E is the number of periods elapsed from the initial epoch. The same ephemeris was used for radial velocity times of maximum (Table 3).

Whenever applicable and possible, the uncertainties of $T_{\rm max}$ were derived by means of the bootstrap method. For samples with small numbers of data points (ANS photometry and the oldest radial velocities), the uncertainties were inferred from the least-squares variance and multiplied by 4. This number was taken from the comparison of uncertainties derived from least-squares and bootstrapping errors for slightly more numerous but still small samples of data. For the data published by van Hoof (1962), the published values of $T_{\rm max}$ were averaged after transferring to the same (mean) epoch, and the uncertainty was estimated as a standard deviation. Finally, the published uncertainties of $T_{\rm max}$ (when no data were available) were multiplied by two as a conservative choice, because usually no details of their derivation were given.

As a by-product of the procedure of the determination of times of maximum light, we obtained amplitudes of the radial mode. The amplitudes are shown in Fig. 5 as a function of $\lambda_{\rm eff}$. A strong increase of amplitude towards short wavelengths, typical for radial modes in β Cep stars, can be seen. In addition, a small amplitude change could have taken place in ξ^1 CMa. For example, the amplitudes in the two BRITE bands are about 25% larger than those derived from the Geneva data. The two data sets are separated by almost three decades, however.

4.3 Correction for the phase lag between light and radial velocity changes

The lag between light and radial velocity data was derived by a trial and error procedure using photometry from SMEI and BRITE and the recent radial velocity measurements. The phase lag is equal to +0.070 ± 0.001 d, corresponding to 0.334 ± 0.005 in phase. This number is very different from a typical value of 1/4, corresponding to the maximum light at the epoch of minimum radius, and observed in other β Cep stars. Even for the two high-amplitude β Cep stars, BW Vul and σ Sco, the phase shifts amount to 0.249 (Pigulski 1993) and 0.265 (Pigulski 1992b), respectively; that is, much less than in ξ^1 CMa.

Nonlinear pulsational calculations indicate that BW Vul is almost certainly a fundamental radial pulsator (Moskalik & Buchler 1994). In this case, the observed standstill in the light curve is caused by an emerging shock wave which originates at the bottom of the He II ionization zone. The first overtone mode is stable.

4.4 Seismic inference from phase lags

The phase lag between light and radial-velocity curves as well as the dependence of phase of the maximum light on wavelength (Fig. 3) can possibly be used to constrain stellar parameters or verify mode identification for the dominant mode. The 4.77 d^{-1} frequency has already been identified as a radial mode by Heynderickx et al. (1994), Cugier et al. (1994), and Saesen et al. (2006) using both photometry and spectroscopy. The strong dependence of amplitude on wavelength (Fig. 5) provides a clear indication that this is the case. However, it was not clear if the mode was fundamental or an overtone although Shultz et al. (2017) showed that the stellar parameters they derived are consistent with the fundamental mode.

We therefore checked if seismic models are able to reproduce the two key observed characteristics: the large phase lag between light and radial-velocity curves, and the phase dependence on wavelength. For this purpose, we calculated a grid of models for stars with stellar parameters close to those provided by Shultz et al. (2017). The models were calculated in the same way as described by Cugier (2014). We used OPAL opacities, hydrogen mass abundances between $X = 0.6$ and 0.8 and two metallicities, $Z = 0.0134$ and 0.0168. Pseudo-rotating, spherically symmetric models (following Soufi et al. 1998) were built assuming rigid rotation with constant total angular momentum during the main sequence evolution. The models were also used to calculate amplitude ratios and phase differences for the Strömgren, Geneva and BRITE photometric systems following the procedure presented by Cugier et al. (1994). We used LTE models calculated by Castelli & Kurucz (2003) (hereafter referred to as CK models) and non-LTE models calculated by Lanz & Hubeny (2007) using the TLUSTY code (Hubeny 1988; Hubeny & Lanz 2011) for microturbulent velocity of $\xi = 2\,{\rm km\,s^{-1}}$ (BG models). The latter grid of non-LTE models has been extended for $\log g > 3.0$ assuming $\xi = 10\,{\rm km\,s^{-1}}$ following the procedure described by Cugier (2012).

The first conclusion that can be drawn from these calculations is that the frequency of the mode for models with masses between 14.0 and 14.5 M$_\odot$ and $T_{\rm eff} = 27$ kK, consistent with parameters of ξ^1 CMa provided by Shultz et al. (2017), can be reproduced only if the radial mode is fundamental. A first overtone can be excluded because: (i) It would require much smaller $T_{\rm eff} \approx 24.5$ kK, which is neither compatible with the spectrum nor the colours of ξ^1 CMa. (ii) It is stable in models. (iii) The theoretical phase lag between light and RV curve is smaller than 0.25 for all models in the considered range of masses, in contrast with the observed value. (iv) As already concluded by Shultz et al. (2017), the stellar parameters they derived are consistent with thes pulsation constant corresponding to the fundamental radial mode. For an overtone, the mass and luminosity inferred from the pulsation constant would be much too high. The second and higher overtones can be excluded for the same

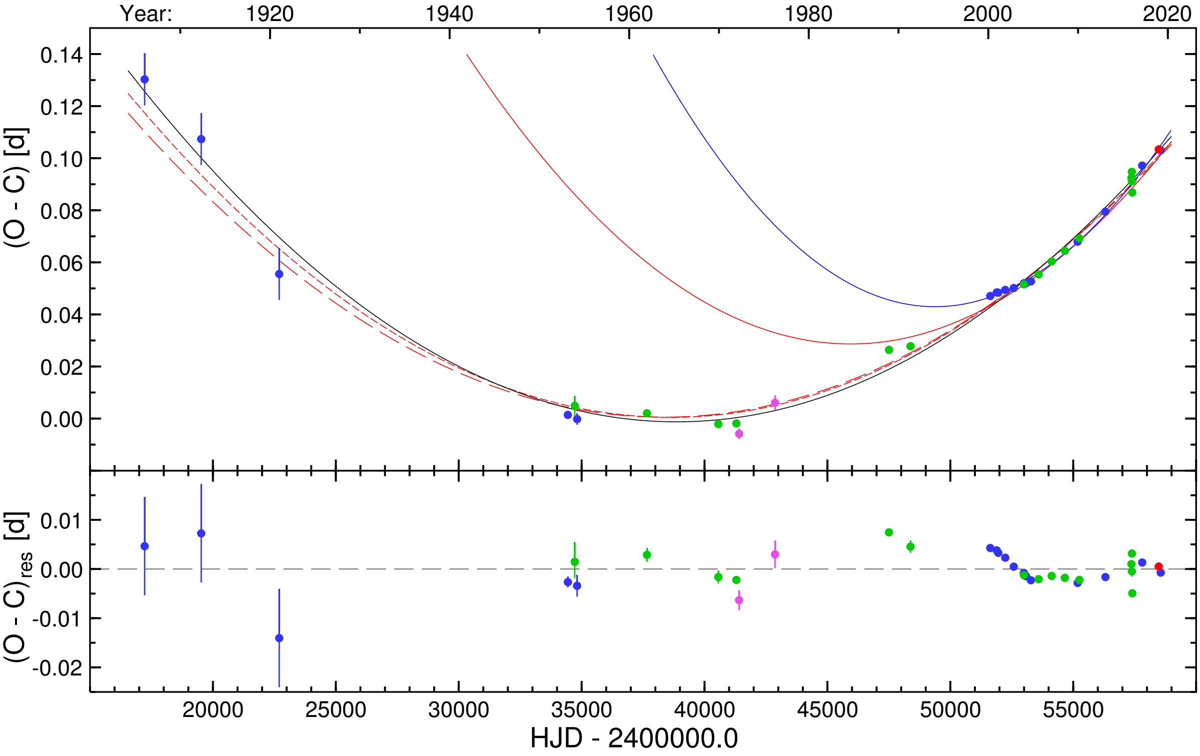

Figure 4. Top: O – C diagram for the light (green dots) and radial velocity (blue dots) times of maximum given in Tables 3 and 4. A constant shift of +0.070 d was applied to the times of maximum radial velocity. Two violet dots correspond to $T_{\rm max}$ derived from TD-1A and ANS UV observations, while the red dot corresponds to $T_{\rm max}$ derived from the TESS data. These three values of O – C are not considered in the fits. Four of the parabolas are fits with different weighting schemes: weights proportional to σ^{-2} (red continuous line), σ^{-1} (red long-dashed line), $\sqrt{\sigma}$ (red short-dashed line) and with equal weights (black line). The blue line shows the fit to the recent (2000 – 2019) RV data only ($\dot{P}$ = 0.97 ± 0.13 s/cen with equal weights). Bottom: residuals from the fit with equal weights.

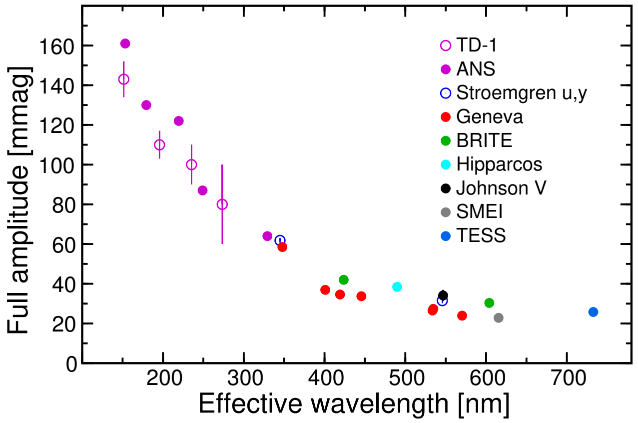

Figure 5. Full amplitudes of the radial mode of ξ^1 CMa. The labels indicate either space mission (TD-1, ANS, Hipparcos, BRITE, SMEI, TESS) or photometric system. The observations can be identified in Table 4.

reasons. Therefore, we conclude that the observed variation corresponds to the fundamental radial mode.

As can be seen in Fig. 3, the wavelength dependence of the photometric phase lags is well reproduced by non-rotating BG models with $M = 14\,M_\odot$, $T_{\rm eff} = 27\,$kK, $X = 0.7042$, $Z = 0.0162$, and $\log g = 3.74$ provided that it is assumed that the mode is radial fundamental. The same models predict phase lags between light and RV curves in the range 0.38 – 0.39, slightly too high in comparison with the observed value. For the non-rotating CK models with $X = 0.7374$ and solar metallicity ($Z = 0.0134$), the phase lag equals to 0.35 – 0.37. Although still slightly higher than the observed value of 0.334 ± 0.005, this value can be regarded as fairly consistent with the observations given the non-sinusoidality of the light curve, which is not reproduced by the models.

4.5 The resulting O – C diagram

The O – C diagram, which uses both photometry and spectroscopy, is shown in Fig. 4. Given the uncertainties of the times of maximum light and radial velocity, the changes of pulsation period cannot be perfectly approximated by a simple parabola corresponding to $\dot{P}$ = const, although such a model is relatively good as a first approximation. The residuals shown in the lower panel of Fig. 4 are much larger than the associated uncertainties (if they cannot be seen, they are smaller than the size of the symbols). Due to the inadequacy of the fitted model, a typical weighting scheme (weights $\propto \sigma^{-2}$) is not the best choice in this case (a large range of uncertainties) leading to large residuals. In total, four different weighting schemes were tried and the results are shown in Fig. 4:

(i) weights $\propto \sigma^{-2}$, $\dot{P} = 0.603 \pm 0.090$ s/cen.

(ii) weights $\propto \sigma^{-1}$, $\dot{P} = 0.325 \pm 0.024$ s/cen.
(iii) weights $\propto \sigma^{-1/2}$, $\dot{P} = 0.338 \pm 0.012$ s/cen.
(iv) equal weights, $\dot{P} = 0.358 \pm 0.008$ s/cen.

The values are consistent with 0.37 ± 0.05 s/cen reported by Jerzykiewicz (1999) and derived by Pigulski (1992a).

As mentioned above, the residuals from the best-fit parabola exhibit scatter that is larger than the uncertainties. In particular, the dense photometric and spectroscopic sampling since the year ~ 2000 is clearly incompatible with the long-term trend, and suggests more complex and rapid period variations. This is confirmed when we attempt to phase these recent measurements using $\dot{P} = 0.3$ s/cen: the measurements are not coherently phased, with clear phase offsets between the datasets. As demonstrated by Shultz et al. (2017) and Begy et al. (2018), a much larger $\dot{P} \sim 0.9$ s/cen rate of period change is needed in order to reconcile them. A period search of the residuals shown in the bottom panel of Fig. 4 yields weak evidence for a period around 40 yr.

5 INTERPRETATION

Examination of the O − C diagram shows that there are two phenomena to be explained: the longer-term increase of the pulsation period at a rate of ~0.3 s/cen, and the more rapid variations detected by Shultz et al. (2017). Because the more rapid changes are diagnosed principally by the modern data, it is unclear if they are a recent phenomenon, or if they existed all along and were only revealed by the recent high-precision observations (although the significant scatter of much of the modern data on the O − C diagram suggests the latter).

In this Section we examine the potential contributions of various phenomena (binarity, stellar evolution, additional (undetected) pulsation modes, and stellar rotation/magnetism) to the long- and short-term evolution of the (apparent) pulsation period.

5.1 Binarity

The light-time effect in a binary system is well known to result in apparent changes of period of orbiting pulsating stars (e.g. Pigulski 1992b). The change in pulsation period is given by:

$$\Delta P = P\,\Delta V_r / c \tag{5}$$

where ΔP is the predicted change of pulsation period P due to light-time effects associated with a radial velocity variation ΔV_r, and c is the speed of light.

Shultz et al. (2017) searched using PIONIER in particular for a Be star companion to ξ^1 CMa. They were able to rule out any companion brighter than 1.7% of ξ^1 CMa's flux (in the *HK* bands) beyond 40 AU, with a similar upper limit derived from the standard deviation of the RVs, within about 40 AU. ξ^1 CMa is reported in the Washington Double Star Catalogue (WDS) to have a companion (V = 14 mag) located at 28″ from the primary. At the Hipparcos distance of ξ^1 CMa (424 pc[11]), one arcsec is 424 AU, so this separation would correspond to nearly 12000 AU. The flux difference is nearly 10 mag in the V band, so we estimate that the companion (assuming it is located at the same distance) would be a K dwarf with a mass of ~0.7 $M_\odot$. The resultant periods are far too long to explain the observed O − C diagram.

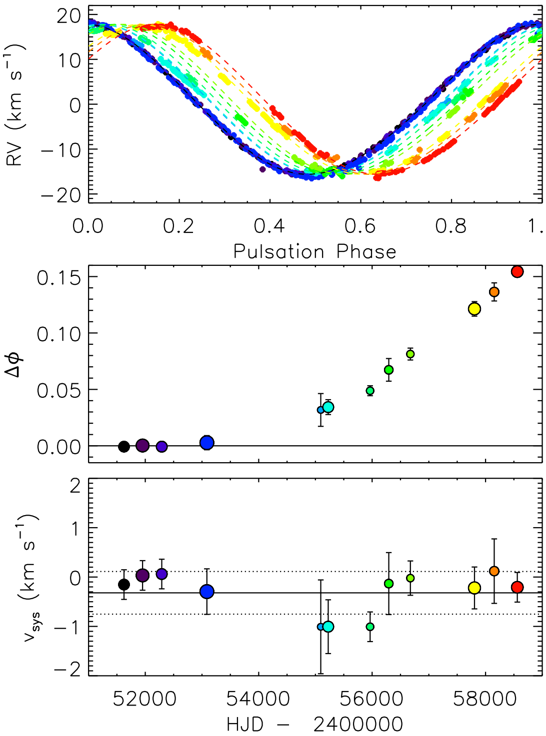

Figure 6. *Top:* CORALIE and ESPaDOnS RVs phased with the pulsation period determined from the first epoch of CORALIE data. Colours indicate time bins. Dashed lines show 3rd-order harmonic fits to the CORALIE data, shifted to minimize the standard deviation of the residuals. *Middle:* phase shift $\Delta\phi$ of the RV curve in each epoch. *Bottom:* systemic velocity $v_{\rm sys}$ determined from the mean residual RV after subtraction of the phase-shifted curves in the top panel. The solid line shows the mean $v_{\rm sys}$, the dotted lines the standard deviations. In the middle and bottom panels, symbol size is proportional to the log of the number of points in each bin.

To attempt to measure the systemic radial velocity $v_{\rm sys}$ of ξ^1 CMa, we fit the RVs from the first year of CORALIE data described by Shultz et al. (2017) with a 3rd-harmonic fit, shifted this curve in phase in each successive two-year bin in order to minimize the standard deviation of the residuals, and then calculated the mean residual RV after subtraction of the curve. The results of this exercise are shown

---

[11] Gaia DR2 gives $\pi = 4.984 \pm 0.346$ mas. This is completely incompatible with the Hipparcos parallax used by Shultz et al. (2017). It is also less precise. At the corresponding distance of about 200 ± 14 pc, the star would have a luminosity of $\log L = 3.83 \pm 0.06$, which at its effective temperature would place it on the Zero-Age Main Sequence, an age at which it would be unlikely to be a β Cep pulsator. As Gaia parallaxes of bright stars ($V \lesssim 6$) should, for the time being, be considered with caution (Lindegren et al. 2018), we adopt the Hipparcos parallax.

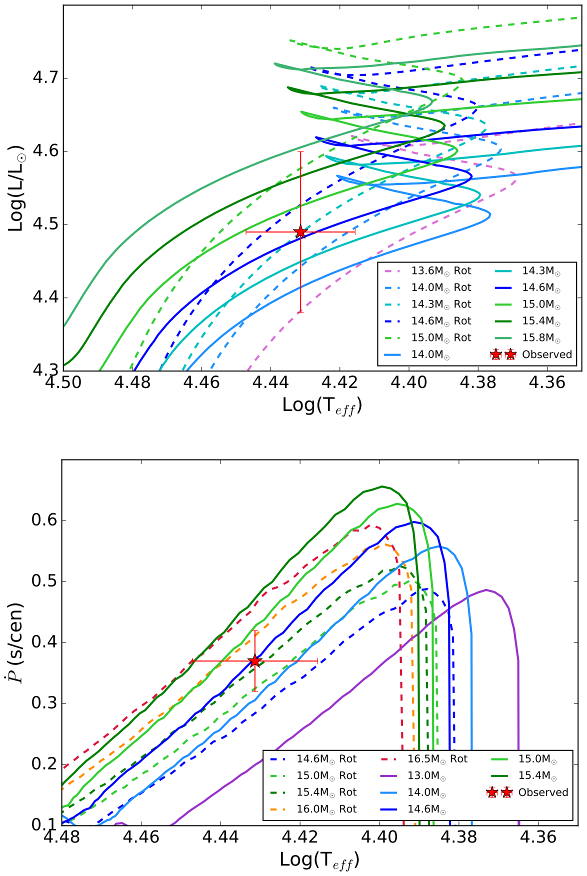

Figure 7. *Upper panel:* Theoretical HR diagram showing evolutionary models ignoring and including the effects of rotation, calculated by Ekström et al. (2012). *Lower panel:* $\dot{P} - T_{\rm eff}$ plane showing the same evolutionary models above, calculated according to Eq.(6) using the evolutionary models. The positions of ξ^1 CMa according to the physical parameters inferred by Shultz et al. (2017) and the rate of period change determined here are shown in red.

in Fig. 6. As can be seen in the bottom panel, the RV curve is consistent with no change in $v_{\rm sys}$ to within about ±0.4 km s^{-1} over the span of observations. If the 0.9 s/cen period change is due to orbital motion, then it should have corresponded to a change in RV of about 3 km s^{-1} over the approximately 20-year span of the RV observations. Since this would have been easily detected, binarity can be ruled out as the source of this period change.

If the 0.3 s/cen period change is due to binarity, on the other hand, we would expect a maximum RV shift of about 1 km s^{-1} over the 20 years covered by these data. Since this is comparable to the standard deviation of $v_{\rm sys}$, orbital motion cannot be excluded in this case. However, there is no positive evidence for a change in $v_{\rm sys}$, and as will be shown below in Sect. 5.2 there is good reason to believe that the 0.3 s/cen period change is due to stellar evolution.

5.2 Stellar evolution

Since the period is growing, this is qualitatively consistent with the increasing radius of the star as expected due to stellar evolution on the main sequence (e.g. Neilson & Ignace 2015). As reported by those authors, the fractional rate of change of the pulsation period of a radially pulsating star due to evolving mass M and radius R on evolutionary timescales can be computed according to:

$$\frac{\dot{P}}{P} = -\frac{1}{2}\frac{\dot{M}}{M} + \frac{3}{2}\frac{\dot{R}}{R}. \tag{6}$$

We have exploited the evolutionary model calculations of Ekström et al. (2012) to predict the variation of $\dot{P}$ according to Eq. (6). Given that ξ^1 CMa is a (relatively) cool upper-main sequence star, its mass-loss rate is expected to be low; hence we have assumed $\dot{M} = 0$ in Eq. (6).

In Fig. 7 we show the star's position on the Hertzsprung-Russell (HR) diagram and on the $\dot{P}$ vs. $T_{\rm eff}$ diagram, using the physical parameters of Shultz et al. (2017) and $\dot{P} = 0.32\pm 0.05$ s/cen, and models both including the effects of rotation ($v_{\rm rot} = 200$ km/s) and ignoring those effects (Ekström et al. 2012) (These tracks bracket potential evolutionary histories of ξ^1 CMa; although the star is known to be a very slow rotator today, the rotational history of the star, and hence the appropriate evolutionary tracks, are unknown.). For the non-rotating tracks, we derive a best-fitting mass of 14.6 M$_\odot$ and age of 9.2 Myr. For the rotating tracks, we derive a best-fitting mass of 14.4 M$_\odot$ and age of 11.1 Myr. The masses are formally consistent with that derived by Shultz et al. (2017). The position on the $\dot{P} - T_{\rm eff}$ is formally consistent with both sets of models. We note that the more recent $\dot{P} \sim 0.9$ s/cen rate of period change does not agree with the models and derived $T_{\rm eff}/\log L$.

5.3 Undetected pulsation modes

To interpret 25-year period variations in the O-C diagram of the β Cep star BW Vul, Odell (1984) submits that a second pulsation mode close in frequency to the primary model could result in the apparent period variation: "An alternate interpretation of the behaviour of BW Vul is in terms of two pulsation modes which are so close to the same period that they don't 'beat' in the normal sense. In this case, the smaller-amplitude mode would have its peak first on the rise up to the peak of the large- amplitude mode, thus making maximum brightness earlier than usual." In the case of BW Vul, the primary pulsation period is very similar to that of ξ^1 CMa, but in our case no obvious O-C periodicity is observed. However, if we assume that the ~40 yr timescale of O-C variability is a result of such a model, then according to Odell (1984) the second mode would differ from the known radial pulsation period by about 0.25 s. In any case, as mentioned by Odell (1984), such unresolved beating should also result in amplitude changes in accordance with apparent period changes. This is not seen for for BW Vul nor ξ^1 CMa.

5.4 Stellar rotation & magnetism

As mentioned earlier, the O-C residuals show weak evidence for a periodic behaviour with $P \sim 40$ years. Such a timescale could be compatible with rotation of ξ^1 CMa. Magnetic early-type stars typically exhibit line profile variability coherent with the rotation period. This can be a consequence of Zeeman splitting, surface chemical abundance peculiarities, or magnetospheric emission. In principle these effects can affect radial velocity measurements. The period change apparent in the more recent data might be oscillatory, and possibly with a decadal timescale; since the rotation period of ξ^1 CMa is extremely long (at least 30 years; Shultz et al. 2017, 2018), it is natural to wonder if some form of rotationally modulated variation might be influencing the radial velocity or light variation of the star.

To investigate this question, we calculated dynamic spectra for various spectral lines using the combined CORALIE and ESPaDOnS dataset. These are shown in Fig. 8. The data were first shifted to zero velocity by subtracting the measured radial velocity, phased assuming a 30-year rotational period with $T_0 = 2455219$ set by the time of maximum $\langle B_z \rangle$, and then co-added in 30 phase bins. Radial velocity correction of individual spectra, combined with the presence of between 16 and about 100 spectra per bin, mean that pulsational variability should be removed to first order. For reference spectra we used the mean spectrum created from the full dataset.

For reference, the top left panel of Fig. 8 shows Hα; this line is already known to exhibit rotationally modulated magnetospheric emission (Shultz et al. 2017). Maximum emission occurs at phase 0 (i.e. at maximum $\langle B_z \rangle$), Shultz et al. 2017, 2018) and the variability pattern is a smooth change in the strength of the central emission feature.

Essentially all of the lines we examined display some form of rotationally modulated variation. The lines shown in Fig. 8 were selected as exemplars of the three different patterns of variability. He II 4686 Å shows a very similar pattern of emission to Hα, suggesting that it is also partly formed within the magnetosphere. O II 4662 Å and Si IV 4116 Å both show a pattern of alternating line strength between the cores and wings, with deeper line cores co-occuring with shallower line wings and vice-versa; the amplitude of the variation is furthermore similar between core and wings. S III 4362 Å and Fe III 5834 Å both show similar patterns of variation, but with the much more pronounced changes in line depth and relatively minor variation in the line wings. All of the metallic lines we investigated showed similar variations, with the lines at their deepest at phase 0, and at their shallowest near phases 0.25 and 0.75 (with the former definitely occurring near $\langle B_z \rangle = 0$).

It is not clear what the source of the metallic line profile variability is. Magnetospheric variation seems unlikely, since: 1) Hα emission is very weak, implying negligible emission in metallic lines; 2) the metallic lines are at peak absorption at phase 0 when (if the variability were magnetospheric in origin) in-filling by emission should be at the greatest. Chemical spots also seem unlikely, as: 1) the formation of surface abundance inhomogeneities is inhibited in B0/B1 stars by their strong(er) winds; 2) all lines vary in essentially the same fashion, whereas the distribution of chemical spots tends to differ from one chemical element to another. Zeeman splitting may be plausible (the expected amplitude in a line with a Landé factor of 1.2, at 5000 Å, for a star with a 1.2 kG surface magnetic field is about 2 km s^{-1}), however this does not seem to be the source of the variation: such splitting should be at its strongest (i.e. line width should be at a maximum) at maximum $\langle B_z \rangle$, whereas precisely the opposite is the case.

The difficulty in explaining ξ^1 CMa's rotationally modulated variation via conventional mechanisms suggests some heretofore unrecognized phenomenon. Whatever the origin of the rotationally modulated variation, however, in all cases it appears to be symmetrical about the line profile; thus, it should have no biasing affect upon the measurement of radial velocities.

6 CONCLUSIONS

We have analyzed spectroscopic and photometric data spanning over a century with the principal goal of examining the pulsation period evolution of the magnetic, slowly-rotating β Cep star ξ^1 CMa. The observations confirm the previously-reported long-term increase of the pulsation period at a rate of approximately 0.3 s/cen, as well as recent, more rapid evolution corresponding to an approximate rate roughly three times larger.

ξ^1 CMa exhibits a number of other characteristics that cause it to stand out from the broader population of β Cep stars. The star exhibits a highly dominant radial pulsation mode, and a century of observations reveals no clear evidence for change in pulsation amplitude. New TESS observations furthermore permit the detection of several low-amplitude modes with frequencies below 5 d^{-1}. As discussed in Sect. 4.3, ξ^1 CMa exhibits a phase offset between maximum light and maximum RV of 0.334, significantly larger than the typical value of ~ 0.25. We demonstrate that these properties can be reconciled by a seismic model in which the star pulsates in the fundamental radial mode. It has the strongest magnetic field of any known β Cep star, and it is one of the most slowly rotating known magnetic stars.

We conclude that the long-term lengthening of the period is not likely a consequence of a binary companion. That rate is however consistent with that expected from evolution of the star at its current position on the main sequence inferred using standard stellar evolution models. We have no particular explanation for the recent, more rapid period evolution, although the associated timescale may be compatible with stellar rotation. Alternatively, we recall that we have observed only a very small part of a phenomenon which may take place on the nuclear timescale. Should we really expect it to proceed so smoothly? Given that the most recent observational data are more precise and provide a much denser temporal sampling, it may well be that similar short-term pulsational accelerations and decelerations have occurred in the past, and that they are a typical phenomenon. In fact, we know of no well-studied β Cep star that shows period evolution with a constant $\dot{P}$ consistent with that expected from stellar evolution models. Period changes in BW Vul, for example, were historically interpreted as a combination of $\dot{P} =$const and light-time effect, but the recent study by Odell (2012) shows the reality can be (much) more complicated. Continued high-cadence monitoring of the pulsation period of the star will be a key to understanding the roles and relationships of these properties in producing the observed period evolution.

ACKNOWLEDGMENTS

Based on data collected by the BRITE Constellation satellite mission, designed, built, launched, operated and sup-

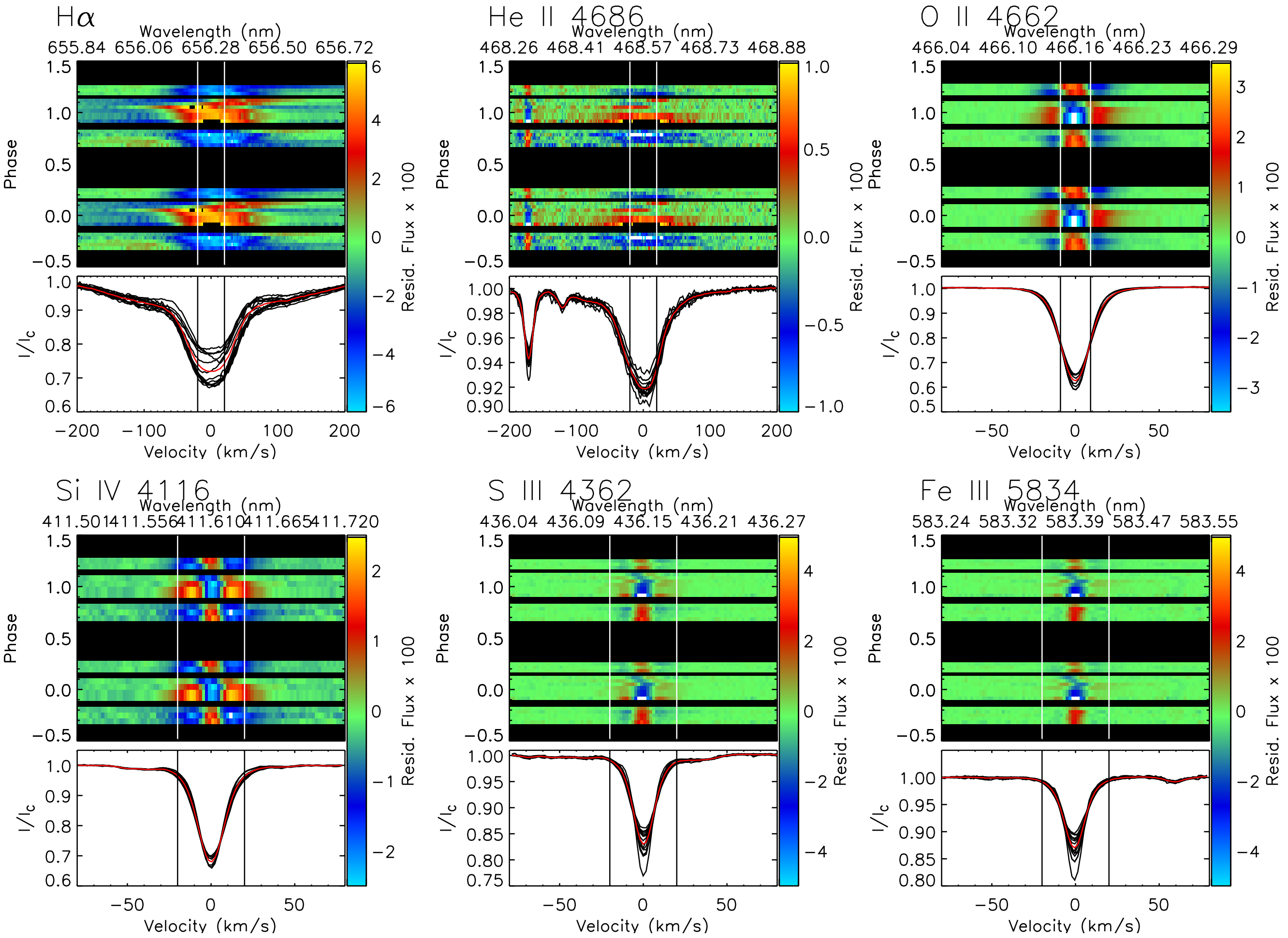

Figure 8. Dynamic spectra displaying line profile variations coherent with the rotational ephemeris of Shultz et al. (2017, 2018). Top panels show residual intensity mapped to colour as a function of rotational phase; bottom panels show phase-binned intensity spectra (black) and the mean reference spectrum (red).

ported by the Austrian Research Promotion Agency (FFG), the University of Vienna, the Technical University of Graz, the University of Innsbruck, the Canadian Space Agency (CSA), the University of Toronto Institute for Aerospace Studies (UTIAS), the Foundation for Polish Science & Technology (FNiTP MNiSW), and National Science Centre (NCN). Based on observations obtained at the Canada-France-Hawaii Telescope (CFHT) which is operated by the National Research Council of Canada, the Institut national des sciences de l'Univers of the Centre national de la recherche scientifique of France, and the University of Hawaii. This paper includes data collected by the TESS mission. Funding for the TESS mission is provided by the NASA Explorer Program. Funding for the TESS Asteroseismic Science Operations Centre is provided by the Danish National Research Foundation (Grant agreement no.: DNRF106), ESA PRODEX (PEA 4000119301) and Stellar Astrophysics Centre (SAC) at Aarhus University. We thank the *TESS* team and staff and TASC/TASOC for their support of the present work. APi acknowledges support from the NCN grant 2016/21/B/ST9/01126, and helpful discussions with Przemek Walczak. Adam Popowicz was responsible for image processing and automation of photometric routines for the data registered by BRITE-nanosatellite constellation, and was supported by statutory activities grant SUT 02/010/BKM19 t.20. GAW acknowledges support from the Natural Sciences and Engineering Research Council (NSERC) of Canada in the form of a Discovery Grant. GH gratefully acknowledges funding through NCN grant 2015/18/A/ST9/00578. We thank Daniel Heynderickx for supplying his photometric data and Monika Rybicka for help with the APT data reduction. KZ acknowledges support by the Austrian Space Application Programme (ASAP) of the Austrian Research Promotion Agency (FFG). MES acknowledges support from the Annie Jump Cannon Fellowship, supported by the University of Delaware and endowed by the Mount Cuba Astronomical Observatory. The authors would like to thank Dr. V. Petit (University of Delaware) and the anonymous referee for helpful comments on the manuscript.

REFERENCES

Anderson R. I., 2018, A&A, 611, L7
Anderson R. I., Sahlmann J., Holl B., Eyer L., Palaversa L., Mowlavi N., Süveges M., Roelens M., 2015, ApJ, 804, 144
Beeckmans F., Burger M., 1977, A&A, 61, 815

Begy S. B., Wade G. A., Handler G., Pigulski A., Sikora J., Shultz M., 2018, in Wade G. A., Baade D., Guzik J. A., Smolec R., eds, 3rd BRITE Science Conference. Proceedings of the Polish Astronomical Society, vol. 8. pp 154–158 (`arXiv:1712.02624`)

Bessell M. S., 2000, PASP, 112, 961

Boksenberg A., et al., 1973, MNRAS, 163, 291

Burger M., Beeckmans F., Kamperman T. M., 1980, A&AS, 39, 301

Campbell W. W., Moore J. H., 1928, Publications of Lick Observatory, 16, 1

Castelli F., Kurucz R. L., 2003, in Piskunov N., Weiss W. W., Gray D. F., eds, IAU Symposium Vol. 210, Modelling of Stellar Atmospheres. p. A20 (`arXiv:astro-ph/0405087`)

Cugier H., 2012, A&A, 547, A42

Cugier H., 2014, A&A, 565, A76

Cugier H., Dziembowski W. A., Pamyatnykh A. A., 1994, A&A, 291, 143

Eddington A. S., 1919, The Observatory, 42, 338

Ekström S., et al., 2012, A&A, 537, A146

Eyles C. J., et al., 2003, Sol. Phys., 217, 319

Fadeyev Y. A., 2015, MNRAS, 449, 1011

Frost E. B., 1907, ApJ, 25, 59

Frost E. B., Barrett S. B., Struve O., 1926, ApJ, 64, 1

Henroteau F., 1921, Publications of the Dominion Observatory Ottawa, 5, 45

Heynderickx D., 1992, A&AS, 96, 207

Heynderickx D., Waelkens C., Smeyers P., 1994, A&AS, 105, 447

Hubeny I., 1988, Computer Physics Communications, 52, 103

Hubeny I., Lanz T., 2011, TLUSTY: Stellar Atmospheres, Accretion Disks, and Spectroscopic Diagnostics (ascl:1109.021)

Hubrig S., Briquet M., Schöller M., De Cat P., Morel T., 2009, in Revista Mexicana de Astronomia y Astrofisica Conference Series. pp CD319–CD322

Jackson B. V., et al., 2004, Sol. Phys., 225, 177

Jerzykiewicz M., 1999, New Astron. Rev., 43, 455

Koopmann R. A., Lee Y.-W., Demarque P., Howard J. M., 1994, ApJ, 423, 380

Kunder A., et al., 2011, AJ, 141, 15

Lanz T., Hubeny I., 2003, ApJS, 146, 417

Lanz T., Hubeny I., 2007, ApJS, 169, 83

Le Borgne J. F., et al., 2007, A&A, 476, 307

Lenz P., Breger M., 2005, Communications in Asteroseismology, 146, 53

Lesh J. R., Wesselius P. R., 1979, A&A, 79, 115

Lindegren L., et al., 2018, A&A, 616, A2

Mathias P., Gillet D., Crowe R., 1991, A&A, 252, 245

McNamara D. H., 1953, PASP, 65, 193

McNamara D. H., 1955, ApJ, 122, 95

McNamara D. H., 1956, PASP, 68, 263

Moro D., Munari U., 2000, A&AS, 147, 361

Moskalik P., Buchler J. R., 1994, in Balona L. A., Henrichs H. F., Le Contel J. M., eds, IAU Symposium Vol. 162, Pulsation; Rotation; and Mass Loss in Early-Type Stars. p. 19

Neilson H. R., 2014, A&A, 563, A48

Neilson H. R., Ignace R., 2015, A&A, 584, A58

Neilson H. R., Engle S. G., Guinan E., Langer N., Wasatonic R. P., Williams D. B., 2012, ApJ, 745, L32

Neilson H. R., Percy J. R., Smith H. A., 2016, Journal of the American Association of Variable Star Observers (JAAVSO), 44, 179

Niemczura E., Daszyńska-Daszkiewicz J., 2005, A&A, 433, 659

Odell A. P., 1984, PASP, 96, 657

Odell A. P., 2012, A&A, 544, A28

Pablo H., et al., 2016, PASP, 128, 125001

Percy J. R., Tan P. J., 2013, Journal of the American Association of Variable Star Observers (JAAVSO), 41, 75

Pigulski A., 1992a, PhD thesis, University of Wrocław (Poland)

Pigulski A., 1992b, A&A, 261, 203

Pigulski A., 1993, A&A, 274, 269

Pigulski A., 2018, in Wade G. A., Baade D., Guzik J. A., Smolec R., eds, 3rd BRITE Science Conference. Proceedings of the Polish Astronomical Society, vol. 8. pp 175–192 (`arXiv:1801.08496`)

Pigulski A., Boratyn D. A., 1992, A&A, 253, 178

Popowicz A., et al., 2017, A&A, 605, A26

Ricker G. R., et al., 2014, in Space Telescopes and Instrumentation 2014: Optical, Infrared, and Millimeter Wave. p. 914320 (`arXiv:1406.0151`), doi:10.1117/12.2063489

Ricker G. R., et al., 2015, Journal of Astronomical Telescopes, Instruments, and Systems, 1, 014003

Saesen S., Briquet M., Aerts C., 2006, Communications in Asteroseismology, 147, 109

Shobbrook R. R., 1973, MNRAS, 162, 25

Shultz M., 2016, PhD thesis, Queen's University (Canada)

Shultz M., Wade G. A., Rivinius T., Neiner C., Henrichs H., Marcolino W., MiMeS Collaboration 2017, MNRAS, 471, 2286

Shultz M., Kochukhov O., Wade G. A., Rivinius T., 2018, MNRAS, 478, L39

Soufi F., Goupil M. J., Dziembowski W. A., 1998, A&A, 334, 911

Strassmeier K. G., Boyd L. J., Epand D. H., Granzer T., 1997, PASP, 109, 697

Wade G. A., et al., 2016, MNRAS, 456, 2

Watson R. D., 1971, ApJ, 170, 345

Weiss W. W., et al., 2014, PASP, 126, 573

Williams A. D., 1954, PASP, 66, 200

van Duinen R. J., Aalders J. W. G., Wesselius P. R., Wildeman K. J., Wu C. C., Luinge W., Snel D., 1975, A&A, 39, 159

van Hoof A., 1962, Z. Astrophys., 56, 141

van Hoof A., Struve O., 1953, PASP, 65, 158

This paper has been typeset from a TEX/LATEX file prepared by the author.